

The Effect of Combustor Exit to Nozzle Guide Vane Platform Misalignment on Heat Transfer over an Axisymmetric Endwall at Transonic Conditions

David Earl Mayo Jr.

Thesis submitted to the faculty of the Virginia Polytechnic Institute and State University
in partial fulfillment of the requirements for the degree of

Master of Science
In
Mechanical Engineering

Wing F. Ng, Chair
Srinath V. Ekkad
Tomas E. Diller

April 1st 2016
Blacksburg, Virginia

Keywords: Experimental Heat Transfer, Transonic, Endwall Aerodynamics, Endwall
Heat Transfer, Computational Fluid Dynamics, Gas Turbines, Secondary Flows

The Effect of Combustor Exit to Nozzle Guide Vane Platform Misalignment on Heat Transfer over an Axisymmetric Endwall at Transonic Conditions

David E. Mayo, Jr.

Abstract

This paper presents details of an experimental and computational investigation on the effect of misalignment between the combustor exit and nozzle guide vane endwall on the heat transfer distribution across an axisymmetric converging endwall. The axisymmetric converging endwall investigated was representative of that found on the shroud side of a first stage turbine nozzle section. The experiment was conducted at a nominal exit M of 0.85 and exit Re 1.5×10^6 with an inlet turbulence intensity of 16%.

The experiment was conducted in a blowdown transonic linear cascade wind tunnel. Two different inlet configurations were investigated. The first configuration, Case I, was representative of a combustor exit aligned to the nozzle platform, with a gap located at the interface of the two components. The second configuration, Case II, the endwall platform was offset in the span-wise direction to create a backward facing step at the inlet. This step is representative of a misalignment between the combustor exit and the NGV platform. An infrared camera was used to capture the temperature history on the endwall, from which the endwall heat transfer distribution was determined. A numerical study was also conducted by solving RANS equations using ANSYS Fluent v.15. The numerical results provided insight into the passage flow field which explained the observed heat transfer characteristics.

Case I showed the typical characteristics of transonic vane cascade flow, such as the separation line, saddle point, and horseshoe vortices. The presence of a gap at the combustor-nozzle interface facilitated the formation of a separated flow which propagated through the passage. This flow feature caused the passage vortex reattach to the SS vane at $0.44 x/C$.

The addition of the platform misalignment in Case II caused the flow reattachment region to occur near the vane LE plane. The separated flow which formed at the inlet step, merged with the recirculation region on the endwall platform, forming two counter-rotating auxiliary vortices. These vortices significantly delayed migration of the passage vortex, causing it to reattach on the SS vane at $0.85 x/C$.

These two flow features also had a significant effect on the endwall heat transfer characteristics. The heat transfer levels on the endwall platform, from -0.50 to $+0.50 Cx$ relative to the vane LE, had an average increase of $\sim 40\%$. However, downstream of the vane mid-passage, the heat transfer levels showed no appreciable heat transfer augmentation due to flow acceleration through the passage throat.

Acknowledgements

First and foremost, I would like to thank my mother Miranda, my aunts, Maureen, Melody, and Michelle; my cousins, Nathaniel and Benjamin as in addition to all of the other members of my family. You have all been with me through the highs and the lows of my life and I would not be the man I am today without the constant and unwavering love and support you have given me.

To my advisor, Dr. Wing Ng, the advice and mentorship you have given me has molded me into the engineer that I am today. Additionally, I would like to thank the other members of my committee, Dr. Srinath Ekkad and Dr. Thomas Diller for their guidance on the research presented herein.

Furthermore, I would like to thank Allan Arisi, James Phillips and Dr. Zhigang Li for their assistance and prior work on this project. The contributions that were made to this project by each of you have immeasurably improved the work presented herein. I would also like to acknowledge the contributions of the ME department's support team, specifically Diana Israel for program support and logistics; Ben Poe and Jamie Archual for their IT support; and Timmy Kessinger, Phillip Long, and Bill Songer for the manufacturing and machining work they provided for the project.

During my time in graduate school, I have learned a great many valuable skills through my interactions with my fellow students. I would like to take the time now to mention a few of these individuals: Andrew Boulanger, Sean Brennan, Jacob Delimont, John Gillespie, Ryan Hehir, John Hutchinson, Matt Murdock, Raul Otero, Jaideep Pandit, and Kevin Peterson.

Finally, I would like to give thanks to our sponsor, Solar Turbines Inc. as well as our contacts within the company, Dr. Hee-Koo Moon and Dr. Luzeng Zhang for trusting us with the task of performing the research presented within.

Table of Contents

List of Figures	vi
List of Tables	viii
Nomenclature	ix
Introduction.....	1
Relevant Past Studies	1
Experimental Study Setup.....	4
Data Reduction Technique.....	7
Numerical Study Setup	8
Numerical Validation.....	9
Case I Endwall Experimental Heat Transfer and Computational Aerodynamics.....	11
Case II Endwall Experimental Heat Transfer and Computational Aerodynamics	14
Computational Endwall Flow Comparison.....	17
Experimental Endwall Heat Transfer Comparison	17
Uncertainty Analysis.....	19
Final Remarks	19
Conclusions.....	20
Acknowledgements.....	20
References.....	21
Appendix A: Endwall Platform Cascade Setup	24
Appendix B: Tunnel Condition Calculation	29
Appendix C: Infrared Technique	31
Appendix D: Linear Regression Data Reduction.....	33
Appendix E: Material Properties Study	35
Appendix F: Uncertainty Analysis.....	36

List of Figures

Figure 1: Virginia Tech Transonic Cascade Wind Tunnel	4
Figure 2: Vane Cascade Geometry	5
Figure 3: Inlet and endwall geometry configurations	6
Figure 4: The vane passage computational domain for Case I.....	9
Figure 5: Endwall static pressure port locations	10
Figure 6: Case I experimental (a) and computational (b) results for surface PR on the endwall	10
Figure 7: Contour of endwall Nu for Case I.	11
Figure 8: Case I span-wise streamlines along plane A-A shown in Figure 9.....	12
Figure 9: Endwall streamlines for Case I.....	12
Figure 10: Case I vortex core visualization near the endwall surface, with the color contour showing pressure ratio on the endwall.....	13
Figure 11: Contour of endwall Nu for Case II.....	14
Figure 12: Case II span-wise streamlines along plane A-A shown in Figure 12.....	15
Figure 13: Endwall streamlines for Case II.	15
Figure 14: Case II vortex core visualization near the endwall surface, with the color contour showing pressure ratio on the endwall.....	16
Figure 15: Percent Nu increase from Case I to Case II.	18
Figure 16: CAD model of test section. The dimensions of the labeled sections are shown in Table A.1.....	24
Figure 17: CAD model of the test section cascade	26
Figure 18: 3D printed vane and endwall pieces.....	27
Figure 19: Image of the assembled test section	28
Figure 20: Endwall exit static pressure port locations in relation to vane geometry.....	29
Figure 21: Positions of the IR window. The left orientation captures the upstream section of the endwall while the right orientation captures the downstream section	31
Figure 22: A CAD drawing of IR window data collection area	32
Figure 23: Least squares linear regression results for a single point	34
Figure 24: Comparison of Nu number plots using ABS supplier material properties (a) and measured material properties (b).	35

Figure 25: Flow chart illustrating how Moffat’s perturbation technique is applied to find the uncertainty in our heat flux results..... 36

List of Tables

Table 1: Cascade Geometry	5
Table 2: Flow Properties	6
Table 3: Test section dimensions	25
Table 4: Exit static pressure port locations as referenced from the leading edge of the upper vane bounding the cascade center passage.....	30
Table 5: Equation E.1 nomenclature.....	37
Table 6: Brown's linear regression uncertainty equation substitutions	37

Nomenclature

C	Chord
c_p	Specific heat at constant pressure
h	Heat transfer coefficient
IR	Infrared
k	Thermal conductivity
LE	Leading edge
M	Mach number
NGV	Nozzle guide vane
Nu	Nusselt number
P	Pitch
PR	Pressure Ratio
PS	Pressure side
q''	Heat flux
Re	Reynolds number (Based on chord length)
SS	Suction side
T	Temperature
t	Time
Tu	Turbulence intensity

Greek

α	Thermal diffusivity
γ	Adiabatic ratio
ρ	Density

Subscripts

1	inlet
2	exit
i	Initial
o	Stagnation
r	Recovery
s	Surface
w	Wall
x	Axial
∞	Freestream

Introduction

The ultimate goal for the gas turbine industry is to generate the greatest amount of power possible for a given turbine size. To achieve the greatest power density, the turbine inlet temperature should be operated at the highest temperature possible. However, doing this presents a considerable challenge to designers as gas turbines have already surpassed the thermal limits of most metals and must be actively cooled to prevent failure. Due to this material limitation, researchers have recently focused on making improvements by modifying the engine geometry. These improvements aim to reduce both thermal heat loads and the effect of secondary flows on the endwall and airfoil.

Many improvements have been made on the nozzle guide vane platform to improve engine efficiency. The development of contoured endwalls to reduce secondary flows across the endwall has reduced both aerodynamic losses through the passage and heat transfer on the endwall platform. Developments in high temperature materials and cooling designs have allowed for combustors to be run at higher temperatures, allowing for increased thermal efficiency.

These improvements have led to unintended design consequences. The large temperature changes that occur as combustion gases pass through the nozzle guide vane lead to misalignments between the combustor exit and endwall platform. This misalignment has the potential to cause an adverse first order effect on the aerodynamic and thermal performance of the engine, leading to a decrease in engine life. The effect of this misalignment on heat transfer across a transonic nozzle guide vane passage is a relatively unexplored field of study for the turbomachinery industry. By investigating this interaction, improvements can be made to current nozzle guide vane endwall designs to mitigate these issues.

Relevant Past Studies

There exists an extensive library of literature on endwall aerodynamics and heat transfer, most of which were done for subsonic conditions and low freestream turbulence. The landmark publications by Herzig et al.[1], Langston [2], as well as those by Goldstein

and Karni [3], Sharma and Butler [4], and Langston et al. [5], among many others, provide detailed insight by means of experimentation and analysis of the flow structures near the endwall platform of a linear cascade. These investigations characterized the nature of cascade blade and vane flows. It was found that the inlet two-dimensional boundary layer near the endwall forms a horseshoe vortex as it encounters the LE of the airfoil. This vortex then splits into two legs, the PS and SS. The stronger PS leg forms the passage vortex and propagates toward the SS of the lower vane, while the weaker SS leg forms the counter vortex on the SS of the vane. As the PS leg lifts off from the endwall, a low speed, three-dimensional, cross flow boundary layer forms in the vane passage. This cross flow moves across the passage from the PS towards the SS of the opposite vane. Overall, it was found that secondary flows are the largest source of aerodynamic losses across the NGV platform.

On the subject of endwall heat transfer, Ames et al. [6], Blair [7], Graziani et al. [8], and Kang et al. [9] each investigated the effect of secondary flows on heat transfer across the NGV passage. From these investigations, it was found that typical areas of high heat transfer include the region near the LE and the entire SS of the airfoil. These locations correspond to the areas where the PS and SS horseshoe vortices have the largest effect on the endwall. The size and strength of these vortices were found to be related to the size of the inlet boundary layer. Additionally, there is a region of relatively low heat transfer that occurs within the passage near the PS of the airfoil. This is associated with the slower cross flow boundary layer which forms as the PS horseshoe vortex leg lifts off from the endwall.

Many other experimental endwall heat transfer studies have been performed at subsonic and low freestream turbulence conditions, including but not limited to, Lynch and Thole [10], Boyle and Russell [11], Boyle and Hoose [12], Thrift et al. [13] and Park et al. [14]. Each of these articles investigate endwall heat transfer under different geometric and/or flow conditions and for each, the major flow field structures and endwall heat transfer distributions associated with them remain present.

Fewer studies have been done for endwall vane heat transfer at transonic and/or high freestream turbulent flow conditions. York et al. [15] and Giel et al. [16] provided baseline transonic endwall pressure loading and heat transfer results at elevated freestream turbulence levels under multiple inlet and exit flow conditions. They found that the heat

transfer on the endwall tends to smoothly increase as the flow propagates through the vane passage.

Radomsky and Thole [17] investigated the effect of high freestream turbulence on endwall heat transfer. It was discovered that an increase in the freestream turbulence intensity induced a significant increase in heat transfer levels over the endwall platform as compared to a case with low freestream turbulence.

More recently, Piggush and Simon [18] conducted heat transfer experiments in a low speed linear NGV cascade with endwall contouring, and misalignment at both the combustor-nozzle interface and slashgap with leakage flow. They found that the addition of a backward facing step with leakage flow reduces heat transfer across the endwall compared to the baseline, no step case. They attributed this decrease to a thickening of the boundary layer on the endwall due to the presence of the step which acts to insulate the wall from the hot mainstream gases.

While much research has been done in recent years regarding endwall heat transfer, there have been relatively few studies in open literature on the effect of combustor-turbine interface misalignment on heat transfer over the NGV endwall. To the authors' knowledge, this study is the first to investigate this effect at transonic, high freestream turbulence conditions with engine representative NGV geometry. The goals of this paper are to present a detailed overview of the effect of interface misalignment on the flow field and heat transfer characteristics of the NGV endwall and to provide a reference for the development and validation of empirical and computational heat transfer models.

Experimental Study Setup

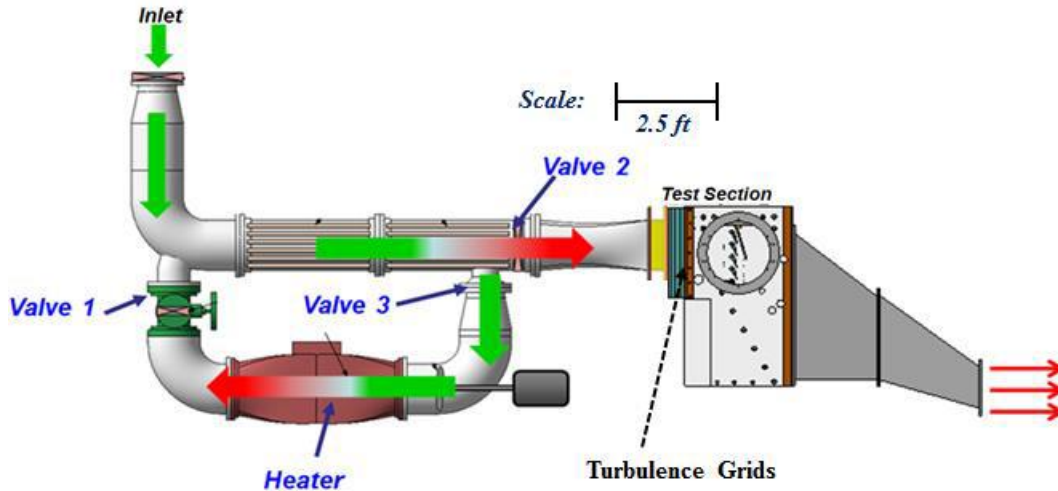


Figure 1: Virginia Tech Transonic Cascade Wind Tunnel

The experiments were conducted in the Virginia Tech Transonic Linear Cascade Wind Tunnel, shown in Figure 1. This blowdown facility is designed to perform steady state aerodynamic and transient heat transfer experiments for up to 15 seconds at a maximum mass flow rate of 4.5 kg/s. Air is supplied from high pressure air tanks that can be charged to a maximum of 1400 kPa. A control valve, located upstream of the test section, regulates the flow of air from the tanks to the test section. Typical cascade inlet pressures range from 20.7 kPa to 82.7 kPa and depend on the cascade geometry and the desired test conditions. The tunnel contains a passive heat exchanger which is used to warm a charge of air to 117° C prior to blowdown. The vane cascade used for this investigation is a 1.5:1 scale model of a land based gas turbine engine. Table 1 summarizes the specifications of the geometry. Figure 1 contains a visual overview of this facility and more details regarding the capabilities of this facility can be found in Anto et al. [19], Holmberg et al. [20], Nix et al. [21], Carullo et al [22], and Nasir et al. [23], among many others.

Table 1: Cascade Geometry

Axial Chord (C_x)	50.0 mm
True Chord (C)	91.2 mm
Pitch (P)	83.1 mm
Span (S)	152.4 mm
Inlet Angle	0°
Exit Angle	73.5°

A Stratasys Fortus 250mc machine was used to print the cascade's vane and endwall components with ABS P-430 material. This material was chosen for its favorable thermal properties ($k = 0.2235 \text{ W/m}\cdot\text{K}$). The endwall parts were manufactured in three pieces and were joined and sealed together in the cascade. This modularity allowed for different endwall geometries to be tested with relative ease. Figure 2 shows an image of the cascade setup.

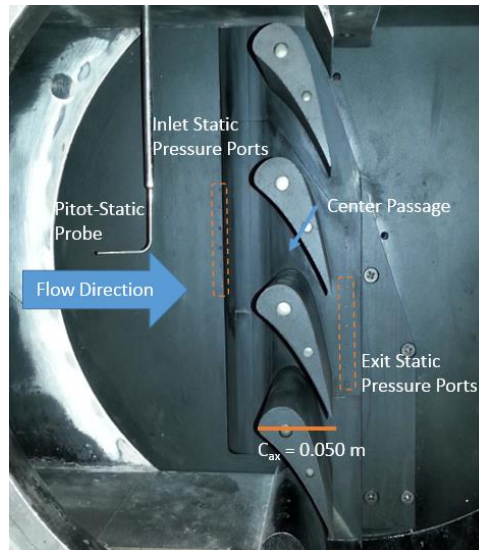


Figure 2: Vane Cascade Geometry

A converging axisymmetric NGV geometry, representative of the endwall located on the casing side of an industrial gas turbine, was used for this investigation. Two different inlet conditions were tested. Case I is representative of a scenario where the endwall platform is in line with the inlet. Case II is an off-design scenario, where the endwall platform is recessed from the inlet, creating a misalignment with the endwall platform.

Figure 3 shows a two dimensional planar cut of endwall geometry and the inlet conditions for the tested cases, where the distance from the leading edge to the step, a , is 43.8 mm and the misalignment, Δ , is 6.78 mm.

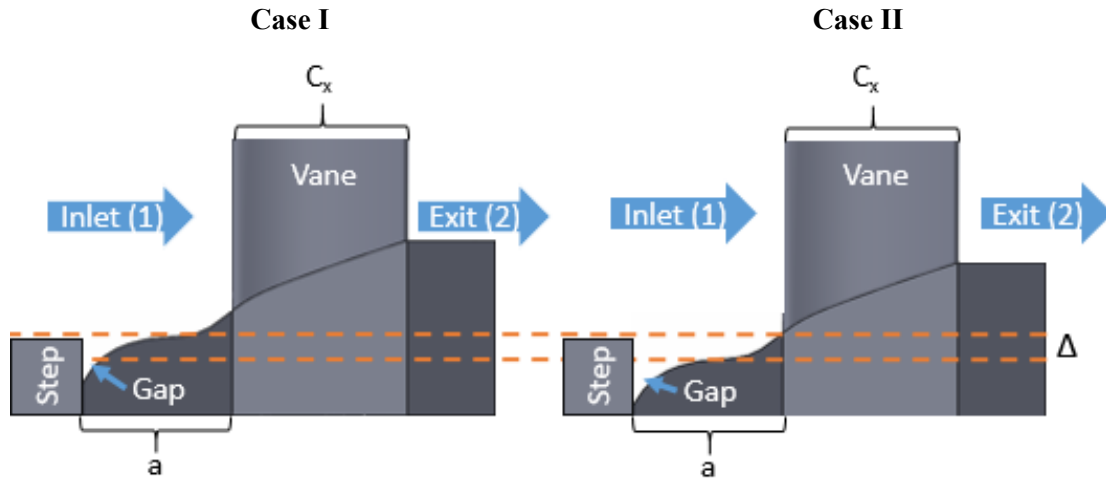


Figure 3: Inlet and endwall geometry configurations

A Model 98RK NetScanner PSI System was used to record pressure measurements during the tunnel run. Six endwall static pressure measurements were taken at both -0.91 and $+1.26 C_x$ relative to the vane's LE (see Figure 2). A pitot-static probe, used to measure the total inlet pressure and static pressure was placed at mid-span and located three C_x upstream of the vane LE. From these measurements, the inlet and exit flow properties were calculated and are given in Table 2. All flow conditions in Table 2, with the exception of the Tu, were recorded at 10 Hz and calculated at each recorded time step. The result was then calculated over a seven second data reduction window. The Tu was measured using a hot-wire anemometry system over 0.6 seconds at 100 kHz.

Table 2: Flow Properties

Inlet Reynolds (Re_1)	5.3×10^5
Exit Reynolds (Re_2)	1.5×10^6
Exit Mach (M_2)	0.85
Turbulence Intensity (Tu)	16%

An accurate measurement of the endwall surface temperature was acquired using a FLIR A325 IR camera. The test section, along with the endwall surface, was painted black to reduce reflections and increase emissivity. Prior to testing, the IR camera was calibrated by the manufacturer.

Data Reduction Technique

The heat flux on the endwall surface is calculated using the Cook-Felderman Method. To use this equation, one must assume a one-dimensional, semi-infinite heat conduction model with a uniform initial temperature throughout the heat transfer domain. For Equation 1, ρ , c_p , and k are respectively the density, specific heat, and thermal conductivity of the solid domain, Δt represents the time step between the previous and the current heat flux calculation, j is the index which corresponds to the measured surface temperature taken at that time step during the run, and n is the total number of surface temperature measurements taken at a single point for the time period of interest. The derivation and details of this method can be found in Cook et al [24].

$$q_w''(t_n) = \frac{2\sqrt{k\rho c_p}}{\sqrt{\pi \Delta t}} \sum_{j=1}^n \frac{T_j - T_{j-1}}{\sqrt{n-j} + \sqrt{n+1-j}} \quad 1$$

A least squares linear regression technique is then used to calculate the h at each measured pixel location on the endwall passage. Newton's Law of Cooling (Equation 2) is modified by including the total temperature of the freestream flow as shown in equation 3. This equation is used in the linear regression technique to determine the h ; where q_w'' is the heat flux, T_∞ is the total temperature of the mainstream flow as measured in the tunnel run, T_w is the surface temperature of the endwall as measured by the IR camera, and T_r is the recovery temperature driving the heat transfer into the endwall. Equation 4 presents a definition of T_r , which varies as a function of Mach number and T_∞ . Since M is held constant for each of our runs, the term in the brackets is a constant, named C_r . Equation 5 is formed by substituting this definition for T_r into Equation 3.

$$q_w'' = h(T_r - T_w) \quad 2$$

$$\frac{q_w''}{T_{t,\infty}} = h \frac{T_r}{T_{t,\infty}} - h \frac{T_w}{T_{t,\infty}} \quad 3$$

$$T_r = T_{t,\infty} \left(\frac{1 + r_c \frac{\gamma - 1}{2} M^2}{1 + \frac{\gamma - 1}{2} M^2} \right) = T_{t,\infty} C_r \quad 4$$

$$\frac{q_w''}{T_{t,\infty}} = h C_r - h \frac{T_w}{T_{t,\infty}} \quad 5$$

The value of the linear regression curve's slope is the heat transfer coefficient and the x-intercept gives the constant C_r , from which the recovery temperature can be derived. A detailed explanation of the data reduction technique can be found in Xue et al [25].

Numerical Study Setup

The Reynolds-Averaged Navier-Stokes Equations (RANS) were solved using ANSYS Fluent v. 15.0 to gain a better understanding of the flow characteristics and their impact on the heat transfer distribution across the endwall. A steady state solver was used, with total pressure and turbulence profiles applied at the inlet as measured from experiments. The fluid domain was modeled as an ideal gas, with thermal conductivity, specific heat, and viscosity being determined using molecular kinetic theory. The Transition-SST turbulence model was used. Figure 4 shows the computational domain for the baseline geometry. Approximately 3 million cells generated using ANSYS ICEM were required to fully resolve the fluid domain, with the maximum $Y^+ < 1$ on the endwall and vane surfaces. This ensured that the viscous sublayer was fully resolved.

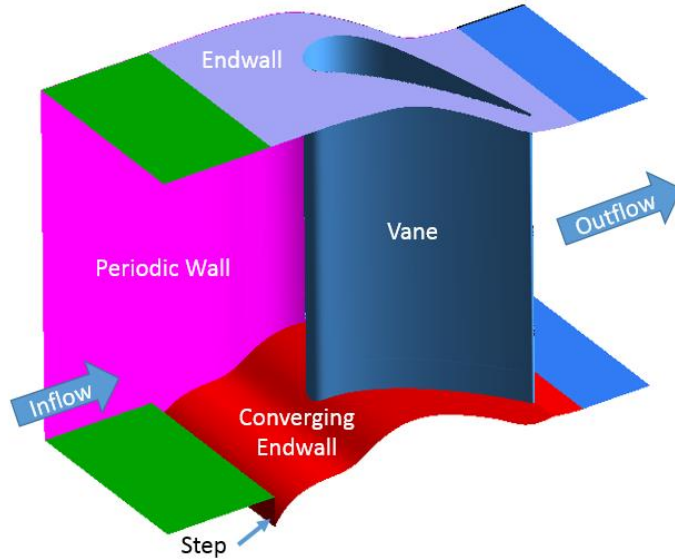


Figure 4: The vane passage computational domain for Case I

Numerical Validation

Experimental static pressure measurements were collected across the endwall at 55 discrete locations, shown in Figure 5, for the Case I endwall configuration. These measurements were used in conjunction with the inlet total pressure measurement to calculate the pressure ratio across the endwall. These measured values were then interpolated across the entire endwall passage for ease of comparison with the computational case.

Figure 6 shows the experimentally measured (a) and computationally calculated (b) pressure loading contours across the endwall for Case I. The magnitudes and gradients in the pressure field agree well between the two data sets. The maximum and minimum error in the pressure values between the two cases are 15% and -16% respectively and occur in the narrowest part of the nozzle passage as where the pressure gradients are largest. The error in this region is exacerbated by the interpolation process. However for the vast majority of the endwall passage, the largest percentage error of the CFD compared to the experimental data is less than $\pm 1\%$.

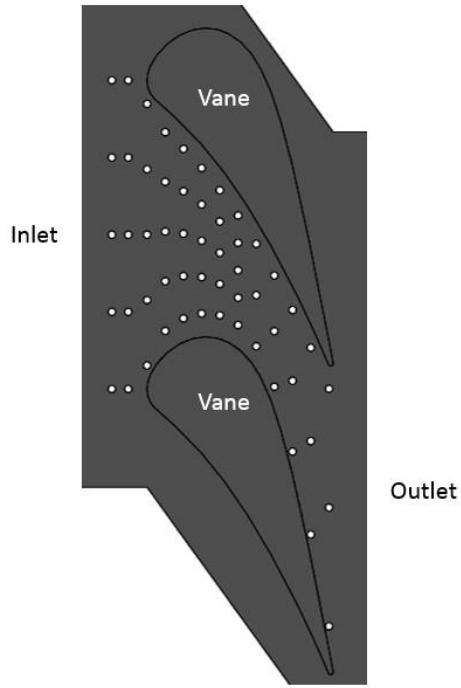


Figure 5: Endwall static pressure port locations

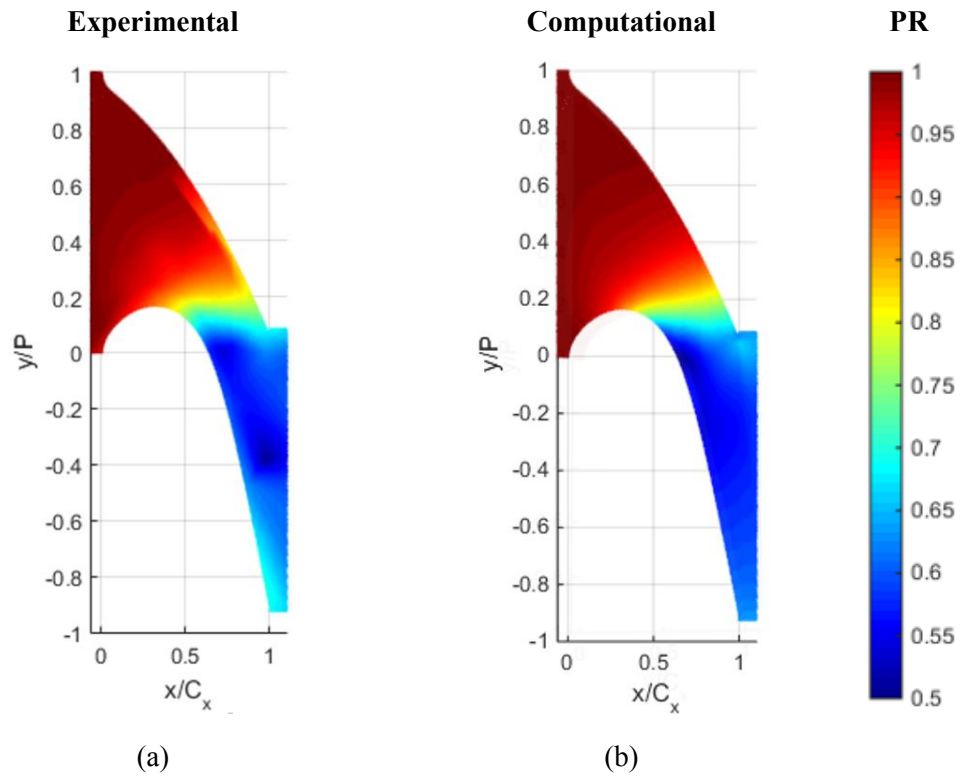


Figure 6: Case I experimental (a) and computational (b) results for surface PR on the endwall

Case I Endwall Experimental Heat Transfer and Computational Aerodynamics

The Case I experimental endwall Nu contour is presented in Figure 7 (a). Downstream of the interface gap, a region of low Nu is present (A). This is due to the pitch-wise recirculation vortices that form in the interface gap, seen in Figures 8 and 10, which insulate the endwall from warmer mainstream flow.

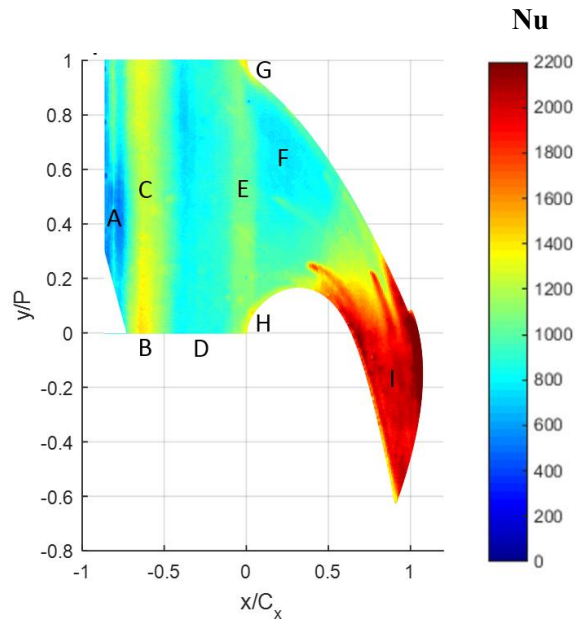


Figure 7: Contour of endwall Nu for Case I.

The Nu increases downstream of this location, from -0.7 to $-0.4 C_x$ (B) due to the reattachment of the mainstream flow to the endwall at $-0.55 C_x$ as observed in Figure 9. The elevated Nu regions immediately upstream and downstream of this point correspond to the formation of two boundary layers at the reattachment line, marked in Figures 8 and 9, each flowing in opposite directions. One boundary layer is driven by flow from the recirculation region and flows upstream. The other boundary layer is associated with the mainstream flow reattachment and moves downstream. Additionally, in this region of elevated Nu, there is an area of slightly lower Nu between $0.4 P$ and $0.7 P$ (C). This is caused by the presence of the separated flow disrupting flow reattachment, shown in Figure 9.

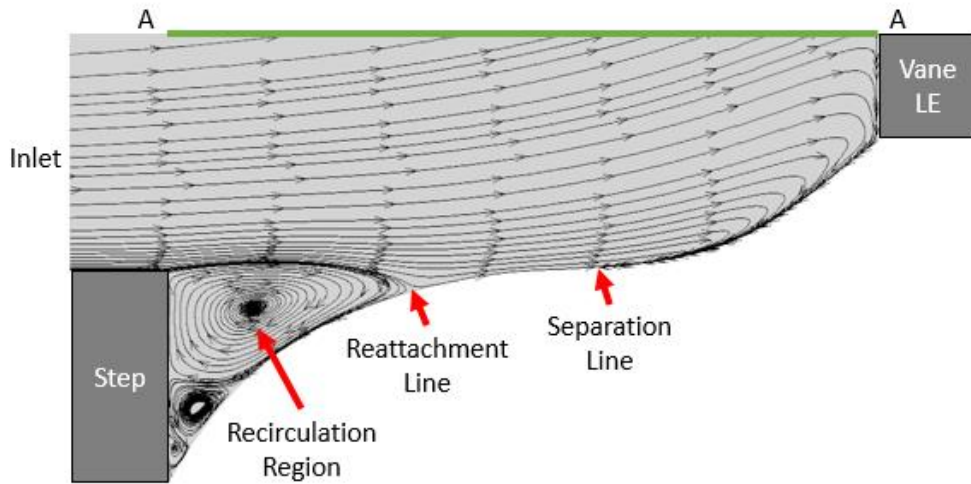


Figure 8: Case I span-wise streamlines along plane A-A shown in Figure 9.

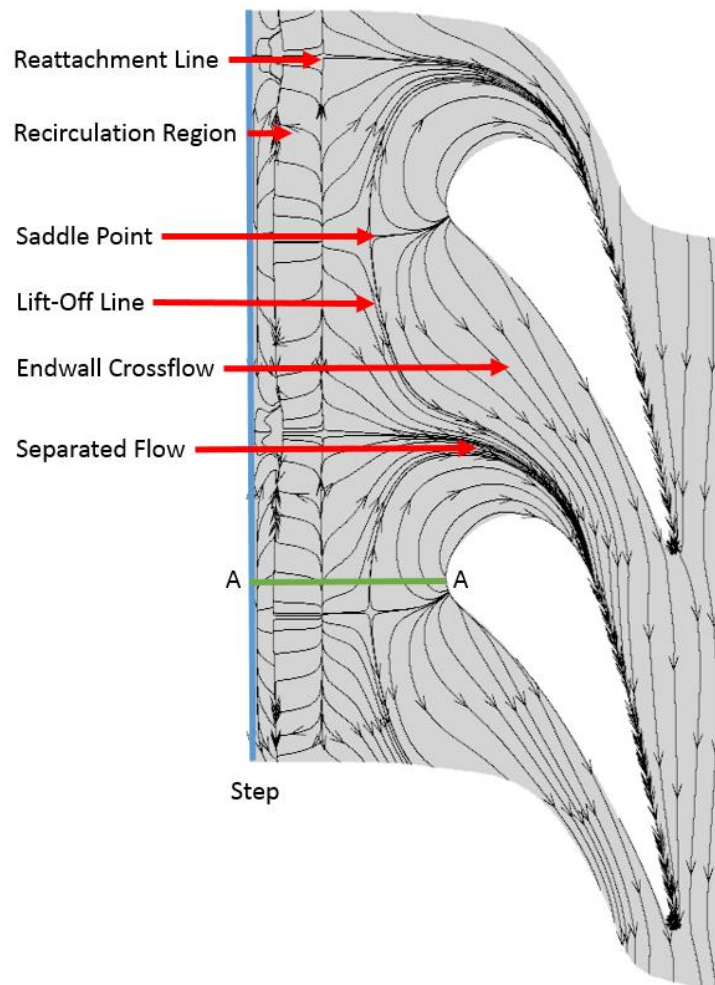


Figure 9: Endwall streamlines for Case I.

Between -0.4 and $-0.1 C_x$ lies a region of relatively low Nu (D). This region is located at the inflection line of the contoured endwall. This is the location where the contour shifts from a convex to a concave curvature. This geometry decelerates the boundary layer flow, increasing its thickness thereby reducing the heat transfer. At the inlet plane of the passage (E) the flow is accelerated, decreasing the boundary layer thickness and increasing heat transfer at the passage LE plane. Downstream of this point, between $+0.1$ and $+0.5 C_x$ (F), there is another region of low heat transfer. This is caused by the cross flow boundary layer that forms when the PS horseshoe vortex lifts off from the endwall, as seen in Figure 9. In the absence of strong vortices in this region, this boundary layer is allowed to grow, insulating the endwall from the hot mainstream gases and reducing the Nu in this region.

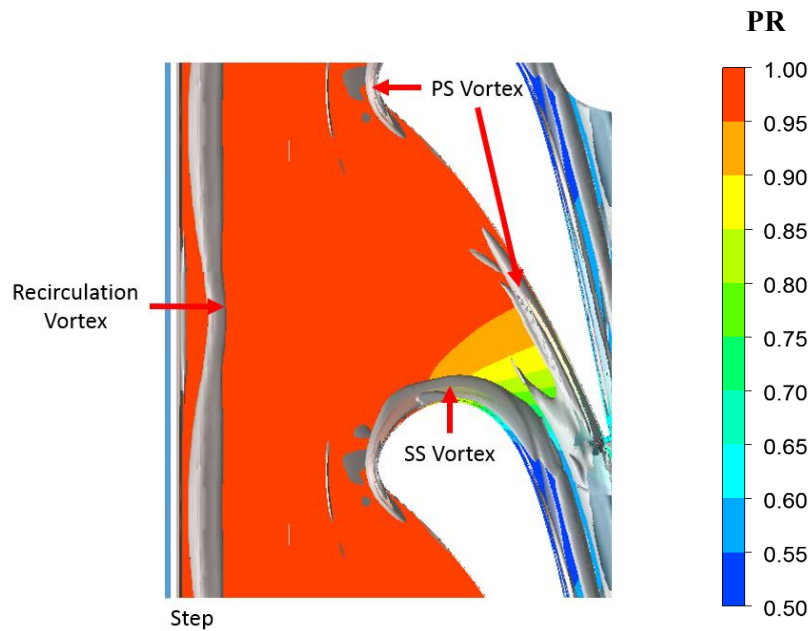


Figure 10: Case I vortex core visualization near the endwall surface, with the color contour showing pressure ratio on the endwall

The high Nu found at the inlet plane of the passage continue along the PS and SS of the vane. This is where the PS (G) and SS (H) legs of the horseshoe vortex are present, seen in Figure 10. Near the exit of the platform (I), the flow accelerates due to the nozzle and endwall contraction, reducing the cross flow boundary layer thickness and increasing the strength of the secondary flows which results in a large increase in heat transfer.

Case II Endwall Experimental Heat Transfer and Computational Aerodynamics

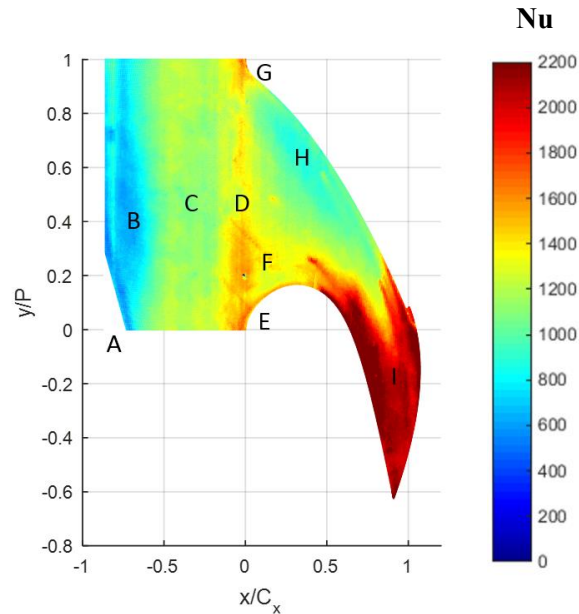


Figure 11: Contour of endwall Nu for Case II.

The Case II experimental endwall Nu contour is also presented in Figure 11. The presence of this step causes the location of mainstream flow reattachment to occur near the inlet plane of the passage, as seen in Figure 12. This creates a large recirculation region across the NGV platform, resulting in significant changes in heat transfer across the endwall.

Downstream of the step, a region of low Nu can be found. This is caused by the secondary flows that occur in the interface gap downstream of the inlet misalignment, shown in Figures 11 and 13. At $\sim 0.4 P$ (A), the low Nu region extends a bit further from the step, forming a bulge. This location corresponds to the location where a separated flow forms, shown in Figure 9. This flow feature pulls the recirculation vortices entrained below the step further into the passage.

There is a significant increase in Nu over the inlet platform between -0.55 and $-0.1 C_x$ (B). This is due to a reverse flow boundary layer formed by the recirculation vortex, seen in Figure 12. At the LE plane of the vane passage (C), the elevated Nu are caused by the flow reattachment at this point.

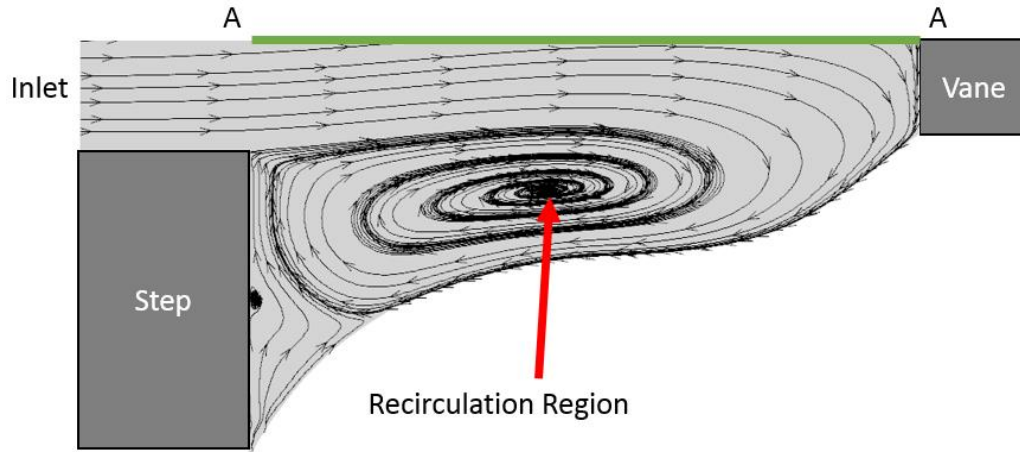


Figure 12: Case II span-wise streamlines along plane A-A shown in Figure 12.

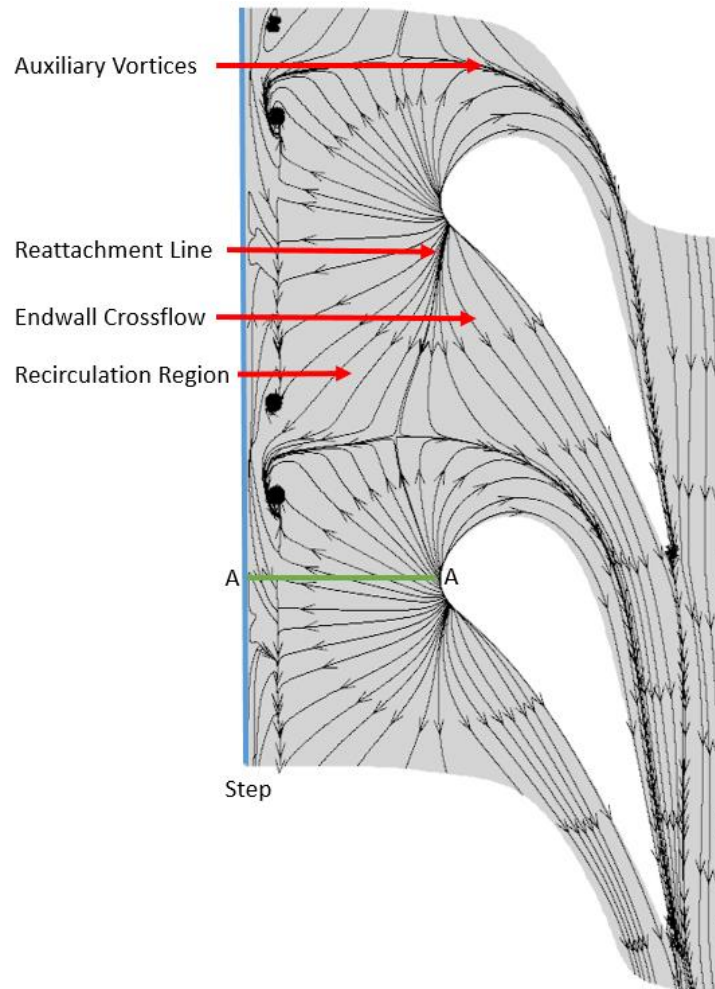


Figure 13: Endwall streamlines for Case II.

On the SS of the vane (D), the high heat transfer can be attributed to the formation of the SS horseshoe vortex, shown in Figure 14. Also in this region, the two counter-rotating auxiliary vortices form due to the interaction between the separated flow at the inlet and the recirculation vortex, as shown in Figure 14. These vortices enter the passage, causing an increase in Nu over the endwall passage (E). Downstream of this location, the Nu increases near the vane's SS as the SS horseshoe vortex merges with the lower auxiliary vortex.

On the PS of the vane, the effect of the PS leg of the horseshoe vortex on the endwall Nu can be seen (F). Moving through the passage, a region of low Nu near the PS surface (G) can be observed. The absence of strong vortices in this region allows for the boundary layer to grow in this region, which leads to a reduction of heat transfer. The acceleration of the flow in the throat increases the strength of the secondary flows in the passage, causing a drastic increase in Nu over the platform in this area (H).

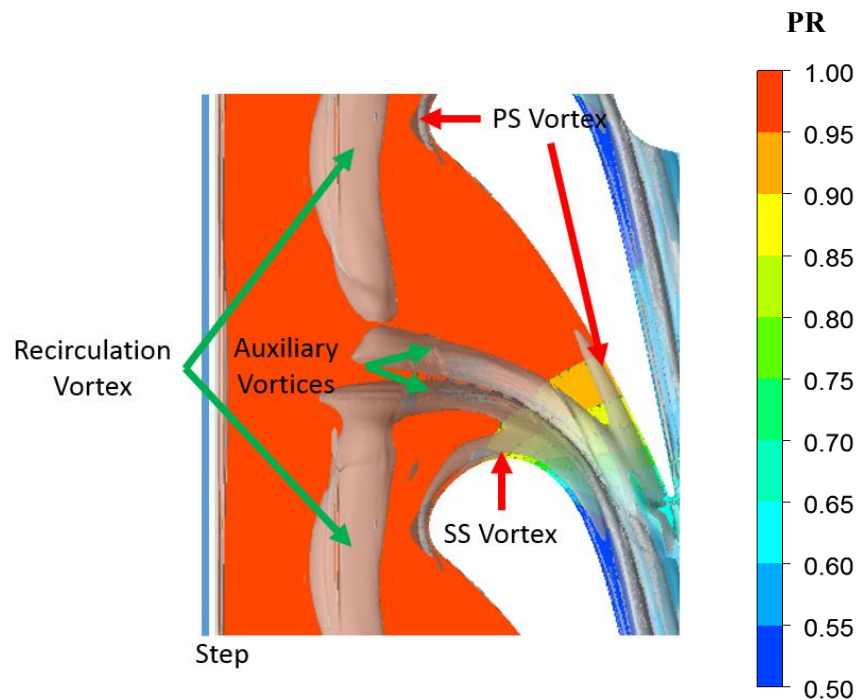


Figure 14: Case II vortex core visualization near the endwall surface, with the color contour showing pressure ratio on the endwall

Computational Endwall Flow Comparison

The upstream misalignment at the cascade inlet generates major differences in the flow field across the endwall platform. All of these differences can be attributed to the shift in the reattachment region caused by this misalignment. The saddle point, which was prominent near the endwall in Case I (Figure 9), is nonexistent in Case II (Figure 13). In Case II, the shift in the reattachment region to the LE plane of the vane passage causes the near endwall flow in this region to propagate upstream. Due to these conditions, near endwall stagnation doesn't occur thus preventing the formation of a saddle point.

Another important difference of note is the delayed migration of the passage vortex. In Case I, the PS leg of the horseshoe vortex is reattaches to the opposite vane at $\sim 0.44 x/C$. In Case II, the PS horseshoe vortex initially merges with the upper auxiliary vortex in the throat of the passage, then eventually with the lower auxiliary vortex. This causes the passage vortex to reattach to the opposite vane at $\sim 0.95 x/C$.

Experimental Endwall Heat Transfer Comparison

To better compare the results from the two cases, the percent increase in the Nu value at each pixel of the image was calculated using Equation 6. The resulting contour is shown in Figure 15. The red colored regions correspond to areas of increased heat transfer and the blue colored regions represent areas of decreased heat transfer from Case I to Case II.

$$\% Nu_{error} = \frac{Nu_{II} - Nu_I}{Nu_I} \times 100\% \quad 6$$

From this analysis, a region of increased heat transfer immediately downstream of the step (A) can be observed. The multiple recirculation vortices that form in Case I, as shown in Figure 8, are not as strong in Case II, shown in Figure 11. The presence of these vortices act to insulate the wall from the mainstream flow, reducing the heat transfer in this region.

Downstream of this location (B), a decrease in the endwall Nu of -20% to -40% occurs. This decrease can be attributed to the difference in size of the recirculation region

for each case. In Case I, the recirculation region ends at $-0.55 C_x$, while for Case II, the recirculation region ends at the LE plane.

Heat transfer on the endwall increases drastically at $-0.5 C_x$ (C). This is due to a shift in the recirculation region from the addition of the backward facing step. The thinner, higher velocity near endwall reverse flow associated with the recirculation region in Case II, as seen in Figure 12, causes an average increase in heat transfer of $\sim 40\%$ over the NGV platform ahead of the vane LE.

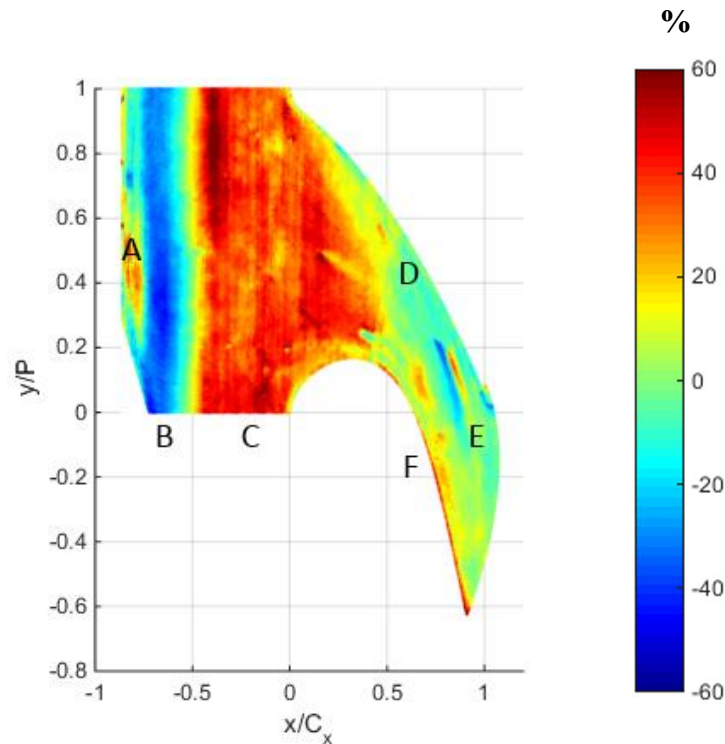


Figure 15: Percent Nu increase from Case I to Case II.

At the mid-chord region near the PS of the vane (D), the difference in the heat transfer values between Case I and Case II drops to $\sim 15\%$. This decrease in the heat transfer differential can be explained by the difference in the size and strength of the PS horseshoe vortex legs. The horseshoe vortex that forms at the vane LE is larger for Case I compared to Case II due to the shift in the flow reattachment location caused by the inlet step. This relative size difference causes the heat transfer near the PS vane to increase faster in Case I compared to Case II. This increase mitigates the difference in Nu between the two cases, resulting in a 15 % decrease in Case II.

As the flow field moves through the passage (E), the difference in heat transfer levels between the two cases drops to less than +5%, with the exception of the region near the suction side surface (F). The small areas of higher Nu near the SS in Case II are associated with the remnants of the auxiliary vortex in Case II propagating through the passage.

Uncertainty Analysis

The uncertainty for this study was calculated using a perturbation technique and a linear regression uncertainty technique presented by Moffat [26] and Brown et al. [27] respectively. The perturbation technique was used to calculate the uncertainty in the heat flux measurement. The average uncertainty calculated using this method was $\pm 6.3\%$. Brown's linear regression uncertainty technique was then used to evaluate the overall uncertainty of the Nu calculation and was found to be $\pm 9.6\%$. This uncertainty calculation is only valid in the regions where the one-dimensional semi-infinite heat conduction model are valid on the endwall

Final Remarks

Piggush and Simon [18] conducted experiments similar to those presented in this paper. In their study, they performed experiments on a case with a backward facing step at the inlet interface with leakage flow. They found reduced heat transfer across the endwall compared to the baseline case, which contained no inlet step. They attributed this decrease to the presence of the step, which shielded the leakage flow from the mainstream flow, allowing the boundary layer associated with it to become thicker.

During the investigation presented in this paper, it was discovered that the backward facing step increased heat transfer across most of the endwall as compared to the baseline case. Since this investigation did not contain leakage flow at the inlet interface, there would be significant differences in the near endwall flow physics, and consequently in the heat transfer distribution across the endwall.

Conclusions

This paper presented a detailed study on the effect of combustor-NGV platform misalignment on heat transfer over an axisymmetric converging NGV. The tests in this investigation were performed in a transonic linear cascade under high freestream turbulence conditions. A numerical investigation was performed on the same geometries to gain insight into the near endwall flow physics which affected the endwall heat transfer.

From this investigation, it was found that the mainstream flow reattachment point for Case II was shifted downstream, to a point just before the vane LE, as compared to Case I. This delays the formation of the new endwall boundary layer and significantly increases heat transfer over significant sections of the NGV platform.

The interface gap at the inlet of the passage causes a separated flow to form. In Case I, presence of the separated flow in the passage causes the passage vortex to reattach at $0.44 x/C$ whereas for Case II, the passage vortex reattachment point is significantly delayed, occurring at $0.95 x/C$.

In Case II, the interaction of the separated flow with the recirculation region facilitates the formation of two counter-rotating auxiliary vortices on the endwall platform. The presence of these vortices, in conjunction with the delayed mainstream flow reattachment, cause an average increase in Nu of $\sim 40\%$ over a significant region of the NGV platform.

Acknowledgements

This work was conducted with the sponsorship of Dr. H. K. Moon and Dr. L. Zhang of Solar Turbines, Inc. The computational work presented in this paper was provided by Dr. Zhigang Li of Xi'an Jiao Tong University.

References

- [1] Herzig, H. Z., Hansen, A. G., and Costello, G. R., 1954, A Visualization Study of Secondary Flows in Cascades, Cleveland, Ohio.
- [2] Langston, L. S., 1980, "Crossflows in a Turbine Cascade Passage," J. Eng. Power, **102**(4), p. 866.
- [3] Goldstein, R. J., and Karni, J., 1984, "The Effect of a Wall Boundary Layer on Local Mass Transfer From a Cylinder in Crossflow," J. Heat Transfer, **106**(2), p. 260.
- [4] Sharma, O. P., and Butler, T. L., 1987, "Predictions of Endwall Losses and Secondary Flows in Axial Flow Turbine Cascades," J. Turbomach., **109**(2), p. 229.
- [5] Langston, L. S., Nice, M. L., and Hooper, R. M., 1977, "Three-Dimensional Flow Within a Turbine Cascade Passage," J. Eng. Power, **99**(1), p. 21.
- [6] Ames, F. E., Barbot, P. a., and Wang, C., 2003, "Effects of Aeroderivative Combustor Turbulence on Endwall Heat Transfer Distributions Acquired in a Linear Vane Cascade," J. Turbomach., **125**(2), p. 210.
- [7] Blair, M. F., 1974, "An Experimental Study of Heat Transfer and Film Cooling on Large-Scale Turbine Endwalls," J. Heat Transfer, **96**(4), p. 524.
- [8] Graziani, R. a., Blair, M. F., Taylor, J. R., and Mayle, R. E., 1980, "An Experimental Study of Endwall and Airfoil Surface Heat Transfer in a Large Scale Turbine Blade Cascade," J. Eng. Power, **102**(2), p. 257.
- [9] Kang, M. B., Kohli, A., and Thole, K. a., 1999, "Heat Transfer and Flowfield Measurements in the Leading Edge Region of a Stator Vane Endwall," J. Turbomach., **121**(3), p. 558.
- [10] Lynch, S. P., and Thole, K. a., 2011, "The Effect of the Combustor-Turbine Slot and Midpassage Gap on Vane Endwall Heat Transfer," J. Turbomach., **133**(4), p. 041002.
- [11] Boyle, R. J., and Russell, L. M., 1990, "Experimental Determination of Stator Endwall Heat Transfer," J. Turbomach., **112**(3), p. 547.
- [12] Boyle, M. T., and Hoose, K. V, 1989, "Endwall Heat Transfer in a Vane Cascade Passage and in a Curved Duct," Volume 4: Heat Transfer; Electric Power; Industrial and Cogeneration, ASME, p. V004T08A009.
- [13] Thrift, A. A., Thole, K. A., and Hada, S., 2011, "Effects of an Axisymmetric

- Contoured Endwall on a Nozzle Guide Vane: Convective Heat Transfer Measurements,” *J. Turbomach.*, **133**(4), p. 041008.
- [14] Park, J. S., Jung, E. Y., Lee, D. H., Kim, K. M., Kim, B. S., Chang, B. M., and Cho, H. H., 2014, “Effects of Unsteady Wake on Heat Transfer of Endwall Surface in Linear Cascade,” *J. Heat Transfer*, **136**(6), p. 061701.
- [15] York, R. E., Hylton, L. D., and Mihelc, M. S., 1984, “An Experimental Investigation of Endwall Heat Transfer and Aerodynamics in a Linear Vane Cascade,” *J. Eng. Gas Turbines Power*, **106**(1), p. 159.
- [16] Giel, P. W., Thurman, D. R., Van Fossen, G. J., Hippensteele, S. a., and Boyle, R. J., 1998, “Endwall Heat Transfer Measurements in a Transonic Turbine Cascade,” *J. Turbomach.*, **120**(2), p. 305.
- [17] Radomsky, R. W., and Thole, K. a., 2000, “High Free-Stream Turbulence Effects on Endwall Heat Transfer for a Gas Turbine Stator Vane,” *J. Turbomach.*, **122**(4), p. 699.
- [18] Piggush, J. D., and Simon, T. W., 2007, “Heat Transfer Measurements in a First-Stage Nozzle Cascade Having Endwall Contouring: Misalignment and Leakage Studies,” *J. Turbomach.*, **129**(4), p. 782.
- [19] Anto, K., Xue, S., Ng, W. F., Zhang, L. J., and Moon, H. K., 2013, “Effects of Tip Clearance Gap and Exit Mach Number on Turbine Blade Tip and Near-Tip Heat Transfer,” Volume 3C: Heat Transfer, ASME, San Antonio, TX, p. V03CT14A005.
- [20] Holmberg, D. G., and Diller, T. E., 2005, “Simultaneous Heat Flux and Velocity Measurements in a Transonic Turbine Cascade,” *J. Turbomach.*, **127**(3), p. 502.
- [21] Nix, A. C., Diller, T. E., and Ng, W. F., 2007, “Experimental Measurements and Modeling of the Effects of Large-Scale Freestream Turbulence on Heat Transfer,” *J. Turbomach.*, **129**(3), p. 542.
- [22] Carullo, J. S., Nasir, S., Cress, R. D., Ng, W. F., Thole, K. a., Zhang, L. J., and Moon, H. K., 2011, “The Effects of Freestream Turbulence, Turbulence Length Scale, and Exit Reynolds Number on Turbine Blade Heat Transfer in a Transonic Cascade,” *J. Turbomach.*, **133**(1), p. 011030.
- [23] Nasir, S., Bolchoz, T., Ng, W.-F., Zhang, L. J., Koo Moon, H., and Anthony, R. J., 2012, “Showerhead Film Cooling Performance of a Turbine Vane at High

- Freestream Turbulence in a Transonic Cascade,” *J. Turbomach.*, **134**(5), p. 051021.
- [24] Cook, W. J., and Felderman, E. J., 1966, “Reduction of data from thin-film heat-transfer gages - A concise numerical technique.,” *AIAA J.*, **4**(3), pp. 561–562.
- [25] Xue, S., Roy, A., Ng, W. F., and Ekkad, S. V., 2015, “A Novel Transient Technique to Determine Recovery Temperature, Heat Transfer Coefficient, and Film Cooling Effectiveness Simultaneously in a Transonic Turbine Cascade,” *J. Therm. Sci. Eng. Appl.*, **7**(1), p. 011016.
- [26] Moffat, R. J., 1982, “Contributions to the Theory of Single-Sample Uncertainty Analysis,” *J. Fluids Eng.*, **104**(2), p. 250.
- [27] Brown, K. K., Coleman, H. W., and Steele, W. G., 1998, “A Methodology for Determining Experimental Uncertainties in Regressions,” *J. Fluids Eng.*, **120**(3), p. 445.

Appendix A: Endwall Platform Cascade Setup

The test section, shown in Figure 16 is constructed out of 6061 aluminum and the two circular windows are made of polycarbonate and their dimensions are given in Table 3. A turbulence grid was located upstream of the test section and generates a measured inlet turbulence intensity of $\sim 16\%$ at $0.48C$ upstream of the cascade leading edge.

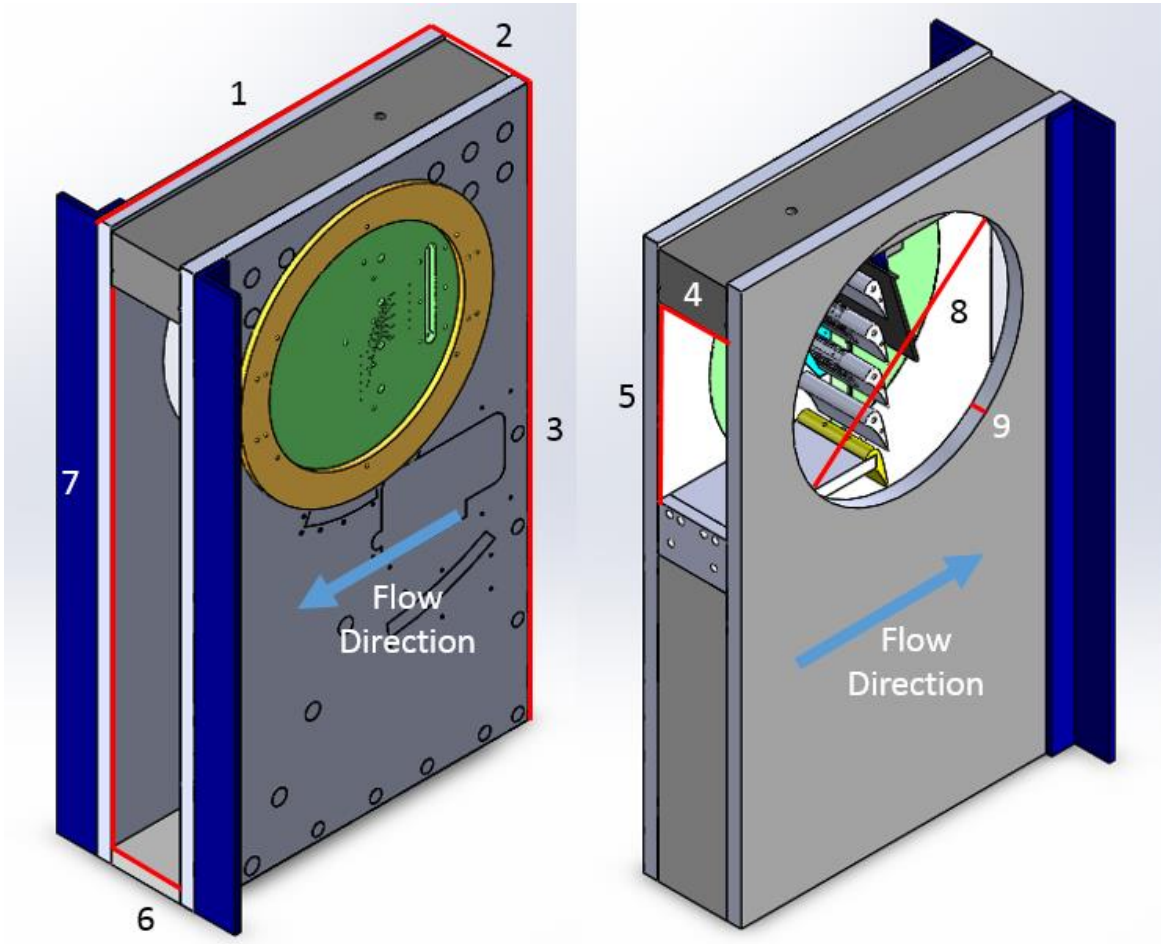


Figure 16: CAD model of test section. The dimensions of the labeled sections are shown in Table A.1.

Table 3: Test section dimensions

	Dimension	Magnitude (m)
Outer Size		
1	Total Length	0.737
2	Total Width	0.216
3	Total Height	1.22
Flow Passage Size		
4	Inlet Width	0.152
5	Inlet Height	0.381
6	Exit Width	0.152
7	Exit Height	0.106
Window Inserts		
8	Diameter	0.508
9	Thickness	0.0318

Figure 17 shows a detailed CAD view of the test section cascade. The test section consisted of five passages with four full vanes. Instrumentation, pressure data and heat transfer data were collected on the central passage (colored green in Figure 2.2). At the start of this research project, pressure data was collected at mid-span of the adjacent vanes to ensure the flow was periodic around this central passage. The dimensions for this cascade have been scaled up to 1.5 times the size of the actual engine geometry. The transition geometry was located 0.0434 m (0.48C) upstream of the leading edge. A parabolic gap geometry was chosen and a step height of 6.78×10^{-3} m (0.267 in) was used based on the average combustor exit and nozzle platform mismatch.

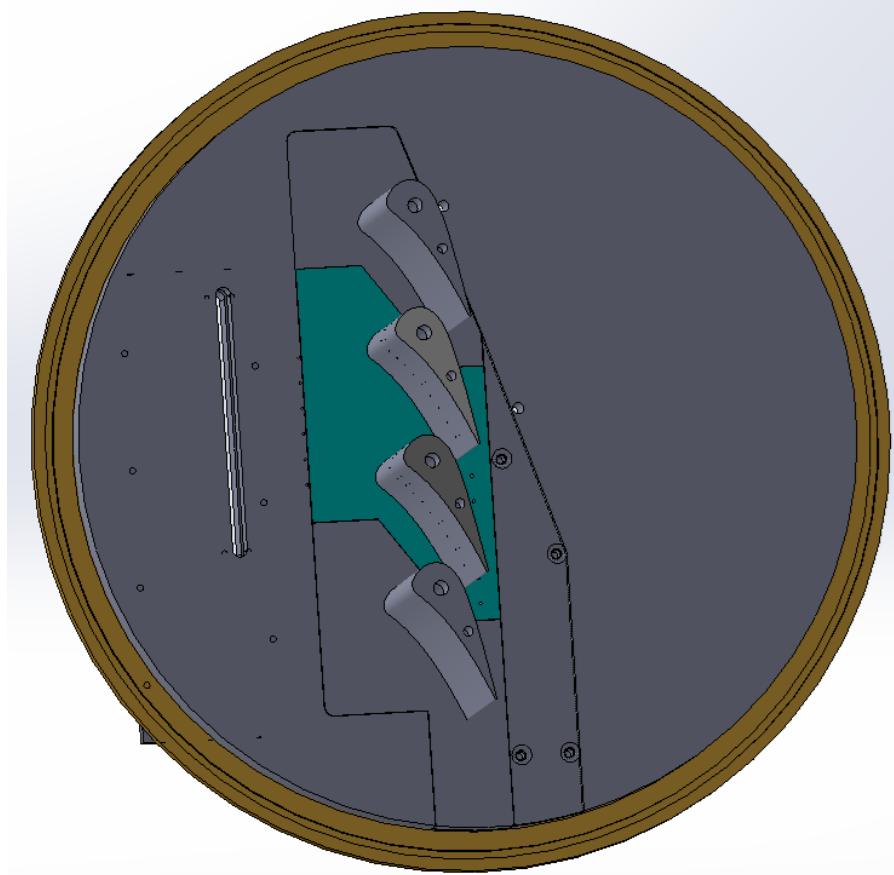


Figure 17: CAD model of the test section cascade

The vanes and endwall were printed adjoined in a Fortus 250mc three-dimensional printing machine by Stratasys using ABS P-430 material which has a low thermal conductivity of 0.2335 W/(m-K). The printed endwall extended approximately 0.0434 m (~0.48 C) upstream of the leading edge, which coincides with the turbine section inlet plane. This configuration allowed for different engine representative NGV endwall platform profiles to be tested in the test section. A slot located one chord upstream of the vane leading edge was used to ascertain the inlet total temperature and total pressure profiles as well as the turbulence conditions. An example of the newly printed plastic vanes and endwall is shown in Figure 18.

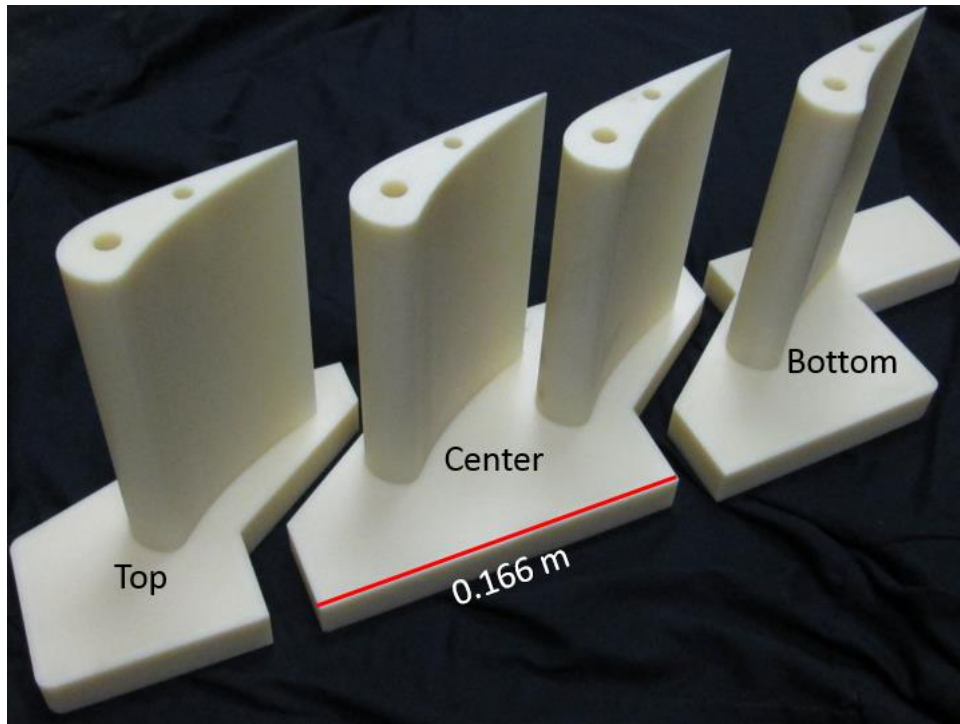


Figure 18: 3D printed vane and endwall pieces.

To prepare the 3D printed parts for testing, the surfaces of all of the parts were lightly sanded, then treated with acetone to obtain a smooth surface finish. The parts were then lightly spray painted black for improved IR measurements. Once the paint dried, the three sections were then bonded together using silicone and JB Weld to prevent leakage through the vane interfaces. The prepared vanes were then inserted into the test section window, which was also prepared with a thin layer of silicone to prevent leakage. The vanes were then secured to the polycarbonate window with screws on the backside.

Twelve 1/16" brass tubes for measuring the cascade inlet and exit static pressure were then inserted into the test section window and secured in place with epoxy. Through the top of the test section, a pitot-static tube is inserted such that the pitot probe tip is located one chord (0.0912 m) upstream of the cascade leading edge, in the center of the inlet flow passage. The assembled test section can be seen in Figure 19.

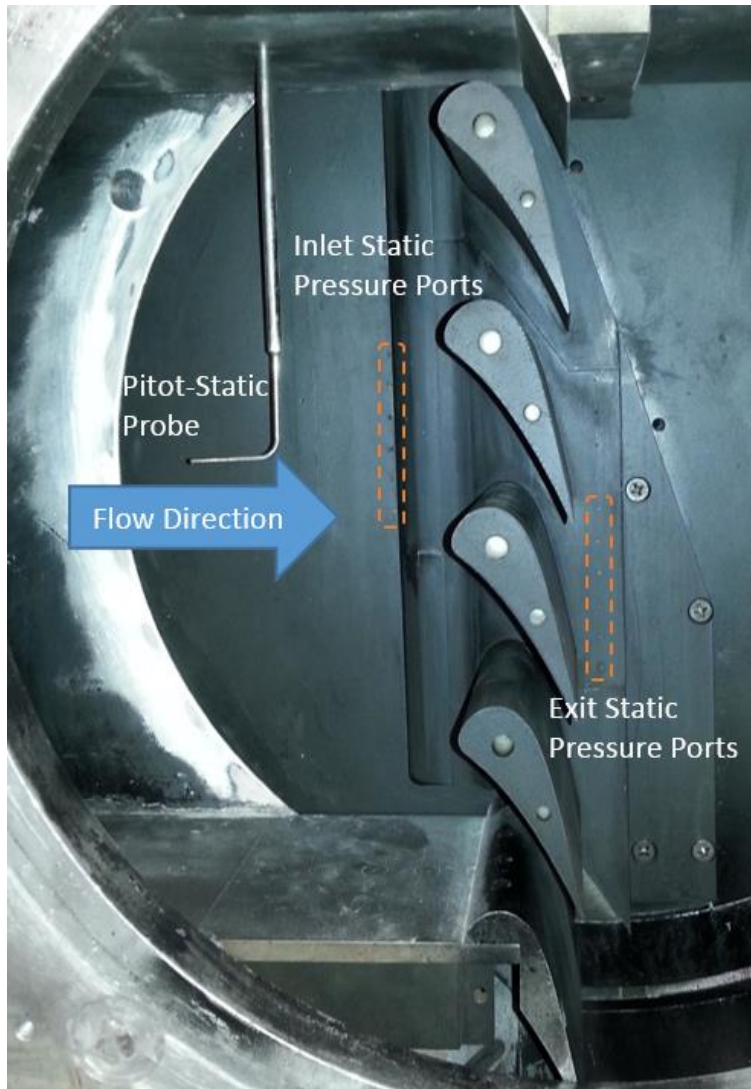


Figure 19: Image of the assembled test section

Appendix B: Tunnel Condition Calculation

Six static pressure ports were placed on the ABS 3D printed endwall downstream of the exit center cascade passage exit plane, as shown in Figure 20. The location of these static pressure ports, as measured from the leading edge of the upper vane bounding the center passage are given in Table 4. The downstream static pressure measurements along with the upstream total and static pressures, measured by a pitot-static tube located one chord upstream of the leading edge, at mid-span and mid-pitch.

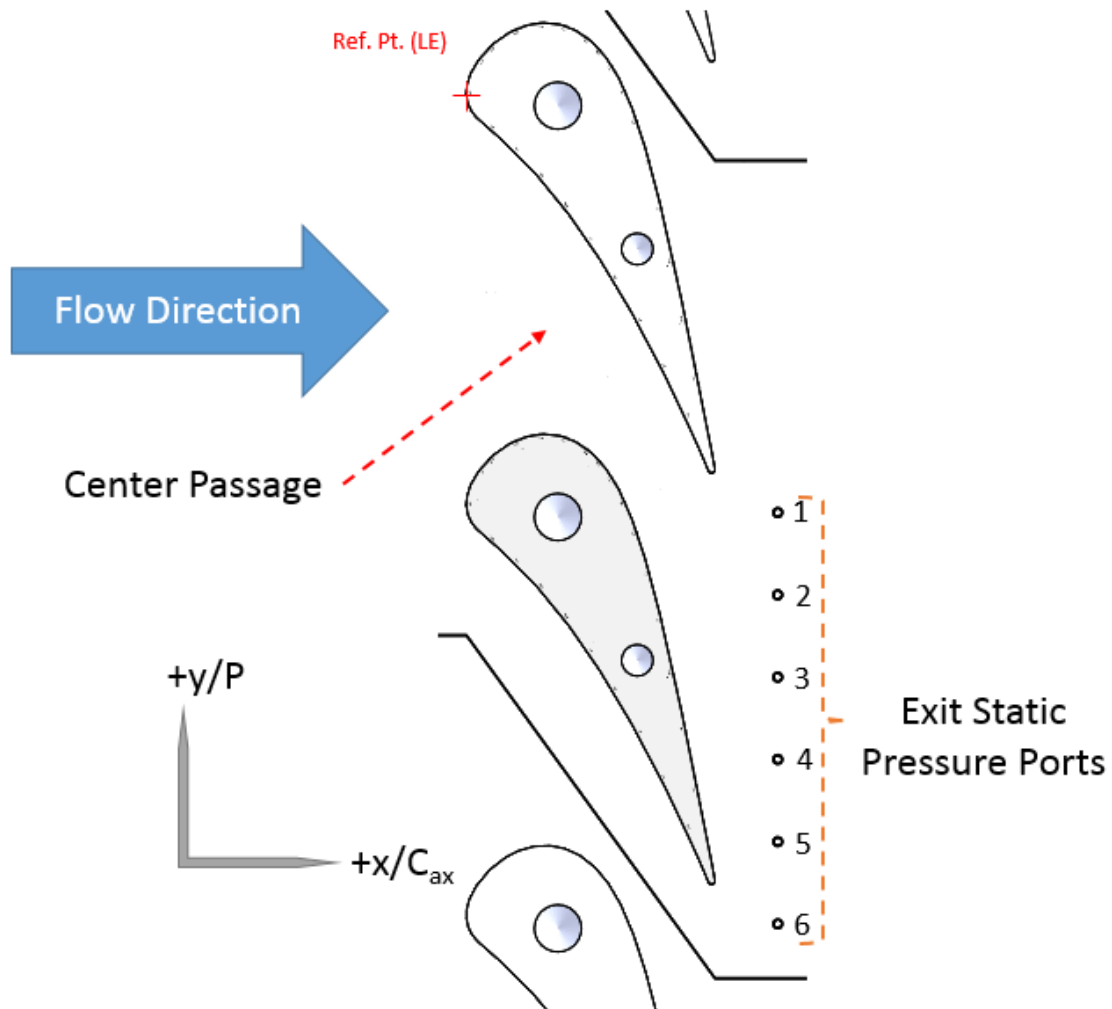


Figure 20: Endwall exit static pressure port locations in relation to vane geometry

Table 4: Exit static pressure port locations as referenced from the leading edge of the upper vane bounding the cascade center passage.

x/C_{ax}	y/P
1.258704	-1.023421
1.258704	-1.223775
1.258704	-1.424129
1.258704	-1.624483
1.258704	-1.824837
1.258704	-2.025191

A Model 98RK NetScanner PSI System is used to record pressure measurements during the tunnel run. The flow through the tunnel is assumed to be isentropic; which means that the total pressure remains constant through the passage. The total pressure for the tunnel run is measured by a pitot-static tube located one chord upstream of the leading edge, placed at mid-span and mid-pitch of the passage ($x/C_{ax} = -1.0$, $y/P = -0.5$). The downstream static pressure measurements from the six pressure taps are averaged at each time step and are used in combination with the upstream total pressure measurement to calculate the exit Mach number at each time step using Equation B.1, where γ is the specific heat ratio of air, P_o is the total pressure and P_s is the static pressure.

$$M = \sqrt{\frac{2}{\gamma - 1} \left(\left(\frac{P_o}{P_s} \right)^{\frac{\gamma - 1}{\gamma}} - 1 \right)} \quad \text{B.1}$$

The upstream Mach number can also be calculated using Equation B.1 and using the upstream static pressure measured by the pitot-static tube. The Mach number is calculated at each time step and is averaged over the seven second data reduction window. This is the reported exit Mach number used for the results presented in this study.

Appendix C: Infrared Technique

An accurate measure of the surface temperature of the endwall throughout the duration of each tunnel run was collected using the FLIR A325 infrared camera. The IR camera uses the blackbody emission radiated from a surface to output that surface's temperature. The test section along with the endwall surface was painted black to reduce reflections and increase emissivity. Prior to testing, the IR camera was calibrated by the manufacturer. To seal the test section a Zinc Selenide (ZnSe) infrared window was installed in the test section, as shown in Figure 20 below. The window has an anti-reflective coating applied and transmits nearly 100% of 9.3 μm wavelength thermal energy. Due to financial constraints, the full set of endwall data had to be collected using two separate runs, one measuring upstream endwall data and one measuring downstream. The positions of these two windows are shown in Figure 21 below. Figure 22 shows the effective viewing area for the endwall after combining the results from the two positions.

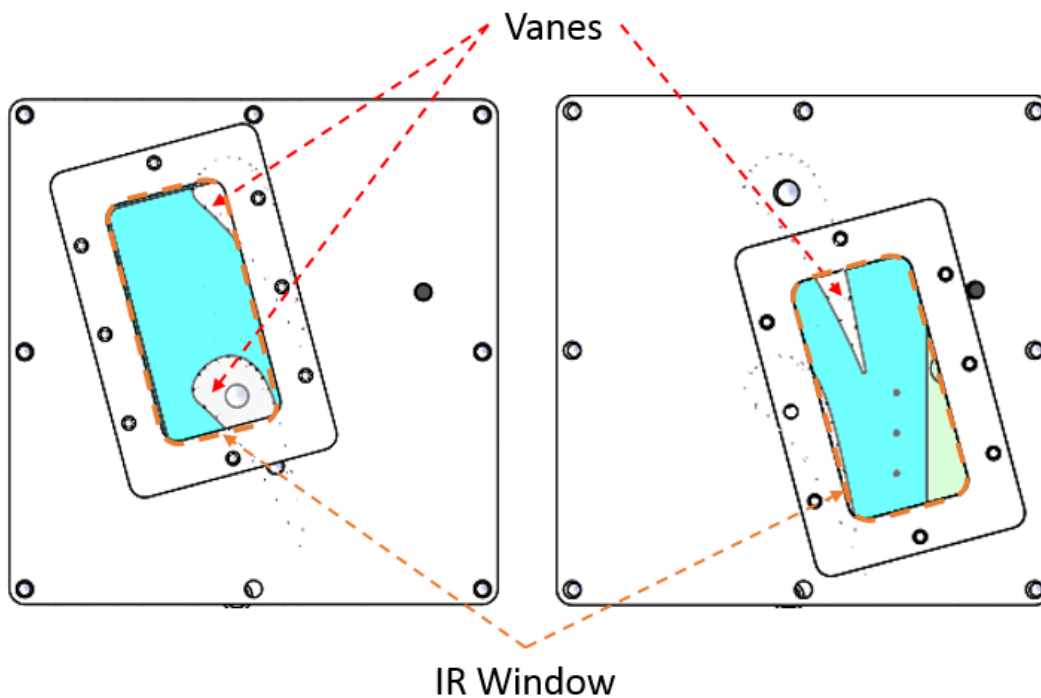


Figure 21: Positions of the IR window. The left orientation captures the upstream section of the endwall while the right orientation captures the downstream section

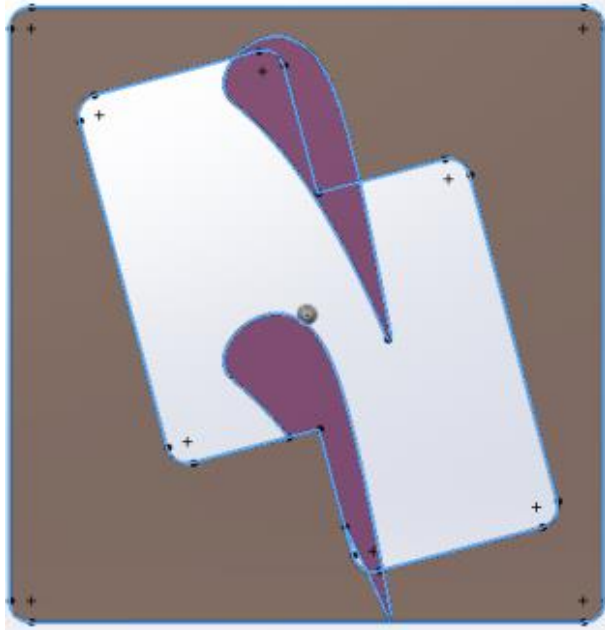


Figure 22: A CAD drawing of IR window data collection area

Appendix D: Linear Regression Data Reduction

The heat flux on the endwall surface is calculated using the Cook-Felderman Method [D.1], shown as Equation D.1 below. To use this equation, one must assume a one-dimensional, semi-infinite heat conduction regime with a uniform initial temperature throughout the heat transfer domain. For Equation D.1, ρ , c_p and k are respectively the density, specific heat, and thermal conductivity of the solid domain, Δt represents the time step between the previous and the current heat flux calculation, j is index which corresponds to the measured surface temperature taken at that time step during the run and n is the total number of surface temperature measurements.

$$q_w''(t_n) = \frac{2\sqrt{k\rho C_p}}{\sqrt{\pi \Delta t}} \sum_{j=1}^n \frac{T_j - T_{j-1}}{\sqrt{n-j} + \sqrt{n+1-j}} \quad \text{D.1}$$

A least squares linear regression technique is used to calculate the heat transfer coefficient, h at each measured location on the endwall passage. Newton's Law of Cooling (Equation D.1) is linearized by including the total temperature of the freestream flow (Equation D.2). This equation is used in the linear regression technique to determine the heat transfer coefficient; where q_w'' is the heat flux, T_∞ is the total temperature of the mainstream flow as measured in the tunnel run, T_w is the surface temperature of the endwall as measured by the IR camera, and T_r is the recovery temperature driving the heat transfer into the endwall. Figure 23 below shows the linear regression curve for a single measurement point on the surface of the endwall. The value of the curve's slope is the heat transfer coefficient. A detailed explanation of the data reduction technique can be found in reference [D.2].

$$q_w'' = h(T_r - T_w) \quad \text{D.2}$$

$$q_w'' = h(T_\infty - T_w) - h(T_\infty - T_r) \quad \text{D.3}$$

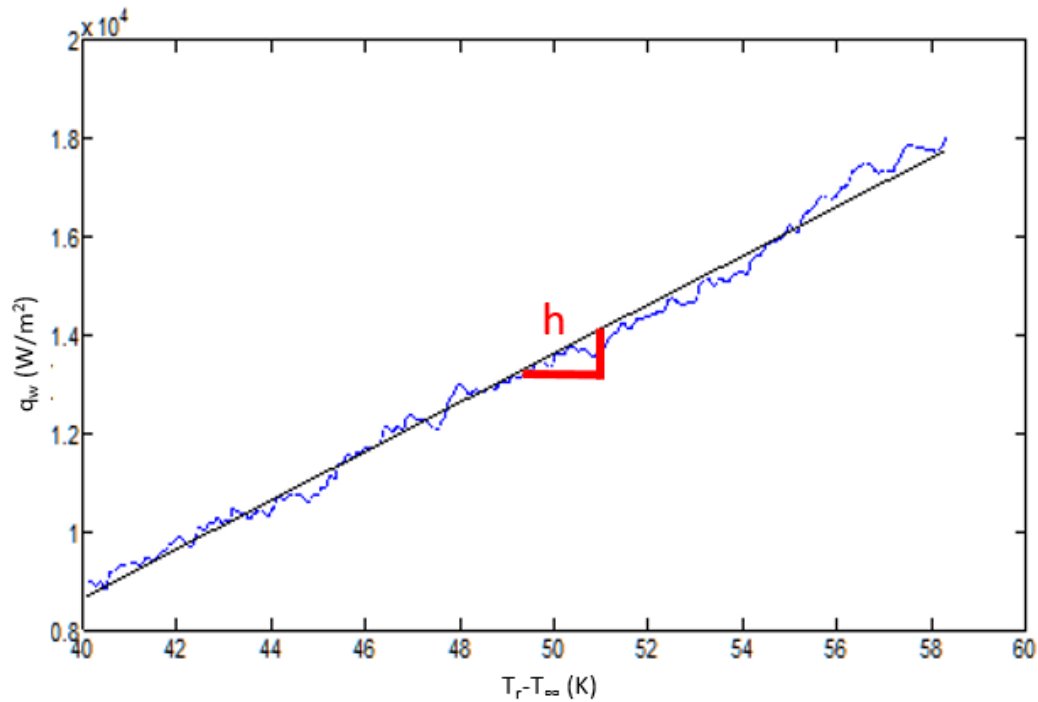


Figure 23: Least squares linear regression results for a single point

References

- [D.1] Xue, S., Roy, A., Ng, W. F., and Ekkad, S. V., 2015, “A Novel Transient Technique to Determine Recovery Temperature, Heat Transfer Coefficient, and Film Cooling Effectiveness Simultaneously in a Transonic Turbine Cascade,” *J. Therm. Sci. Eng. Appl.*, **7**(1), p. 011016.
- [D.2] Cook, W. J., and Felderman, E. J., 1966, “Reduction of data from thin-film heat-transfer gages - A concise numerical technique.,” *AIAA J.*, **4**(3), pp. 561–562.

Appendix E: Material Properties Study

The thermal material properties used to deduce the heat transfer data were obtained from the supplier of the ABS P-430 3D printing plastic. However, in order to ascertain that these properties were valid after the parts had been printed, a sample of the printed part was sent to an outside vendor to establish its thermal properties within the temperature ranges (~25°C to ~100°C) which the experiments are conducted. A comprehensive copy of results can be found on a separate document attached with this report.

An average of the material properties between the temperature range of 25°C and 75°C was used to determine if there was any significant effect of the calculated endwall heat transfer. The result is shown in Figure E.1 below. It can be noted that, while there is some variability in the individual material properties between the ABS supplier specifications and the experimentally verified measured properties, the overall difference on thermal diffusivity is minimal and negligible. As a result no significant variation was noted on the calculated surface heat transfer, as can be seen in Figure 24.

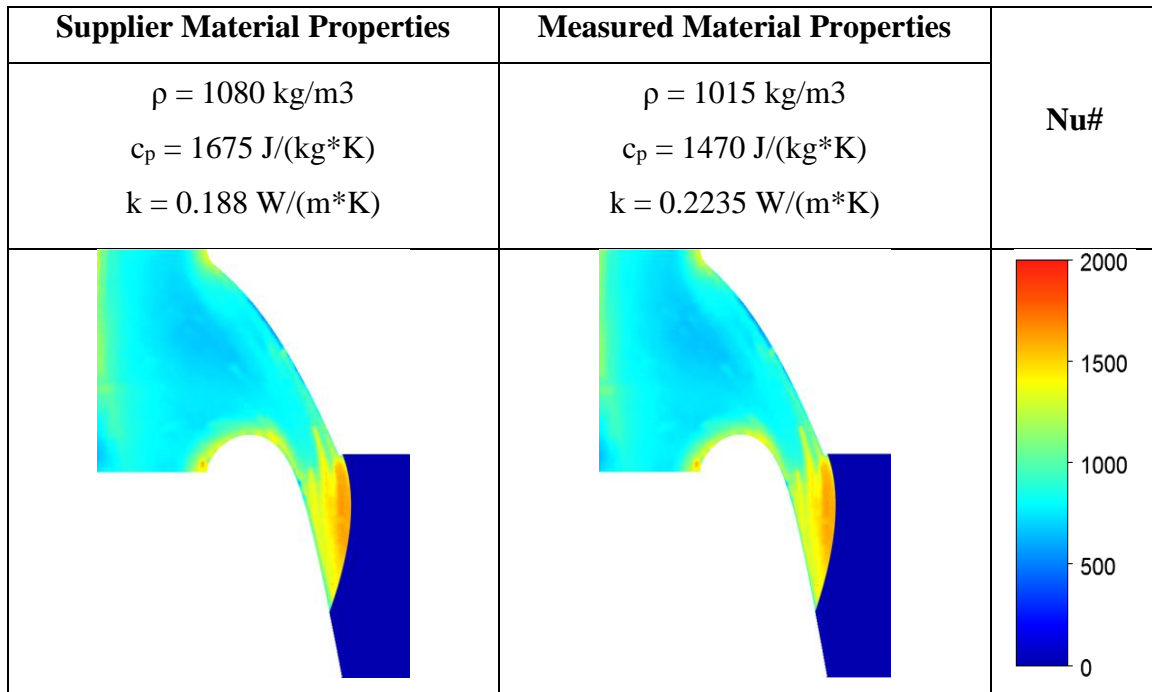


Figure 24: Comparison of Nu number plots using ABS supplier material properties (a) and measured material properties (b).

Appendix F: Uncertainty Analysis

In this appendix, the technique used to characterize the uncertainty in the heat transfer results presented in this study will be discussed. A two-fold approach was used for this study, a perturbation technique described by Moffat et al. [F.1] and a linear regression technique presented by Brown et al. [F.2].

Moffat's perturbation technique was used to calculate the uncertainty in the surface heat flux calculated from the endwall surface temperatures. To do this, the temperatures as measured by the IR camera were increased by an amount equal to the uncertainty in the IR camera's measurement capabilities. The heat flux was then calculated using this perturbed temperature value using the Cook-Felderman equation. The diagram presented in Figure 25 presents a flowchart of Moffat's uncertainty technique as applied to our data.

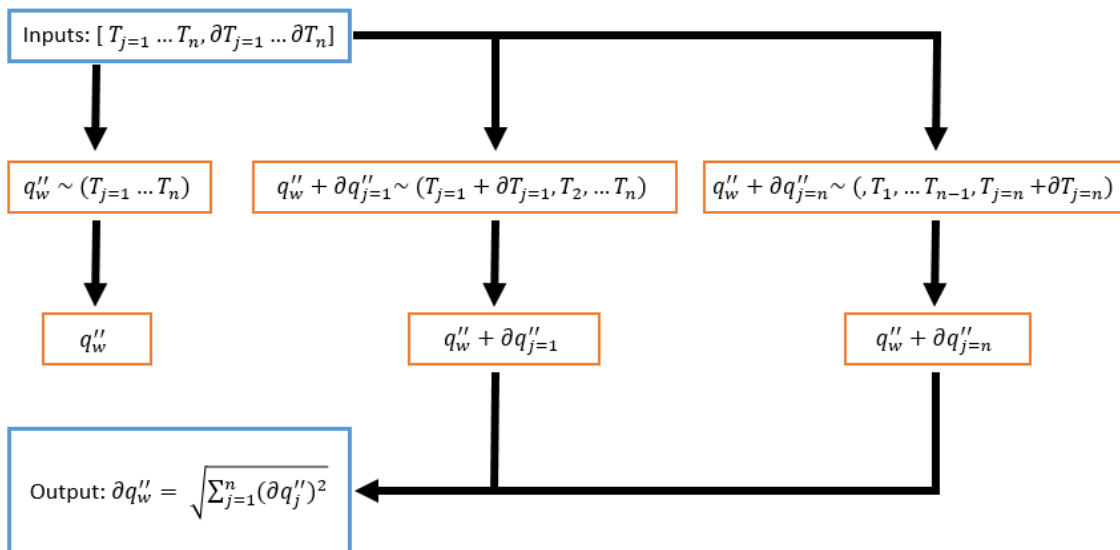


Figure 25: Flow chart illustrating how Moffat's perturbation technique is applied to find the uncertainty in our heat flux results.

Once the uncertainty in the heat flux has been determined, the uncertainty in the HTC, which is derived from the heat flux, can be determined. This is done using Brown's regression uncertainty technique [F.2]. This technique finds the uncertainty in a parameter which is found through a linear regression analysis. In this case, the uncertainty for the heat transfer coefficient, represented by the slope of the linear regression line, is desired.

For a given regression scheme with known x and y values, the uncertainty in a

desired parameter, m , is given by Equation E.1. This equation holds true for a large sample size and is valid given a 95% confidence interval. The definitions of the variables in Equation E.1 can be found in Table 5. To find the HTC, the substitutions given in Table 6 can be used in Equation E.1.

$$\begin{aligned}
 u_m^2 = & \sum_{j=1}^n \left(\frac{\partial m}{\partial y_j} \right)^2 P_{yj}^2 + \sum_{j=1}^n \left(\frac{\partial m}{\partial x_j} \right)^2 B_{xj}^2 + \sum_{j=1}^n \left(\frac{\partial m}{\partial x_j} \right)^2 P_{xj}^2 + \sum_{j=1}^n \left(\frac{\partial m}{\partial x_j} \right)^2 B_{xj}^2 \\
 + 2 \sum_{j=1}^{n-1} \sum_{k=i+1}^n & \left(\frac{\partial m}{\partial y_j} \right)^2 \left(\frac{\partial m}{\partial y_k} \right)^2 B_{yj}^2 B_{yk}^2 + 2 \sum_{j=1}^{n-1} \sum_{k=i+1}^n \left(\frac{\partial m}{\partial x_j} \right)^2 \left(\frac{\partial m}{\partial x_k} \right)^2 B_{xj}^2 B_{xk}^2 \\
 & + 2 \sum_{j=1}^n \sum_{k=1}^n \left(\frac{\partial m}{\partial y_j} \right)^2 \left(\frac{\partial m}{\partial x_k} \right)^2 B_{yj}^2 B_{xk}^2
 \end{aligned} \tag{E.1}$$

Table 5: Equation E.1 nomenclature

B	Bias Limit
$B_{ik}=B_i B_k$	Covariance Estimator
m	Line slope
n	Number of data points
P_{xj}, P_{yj}	Random number uncertainty
u	uncertainty
x	Independent variable
y	Dependent variable

Table 6: Brown's linear regression uncertainty equation substitutions

Equation Variable	Substituted Variable
x	$-\frac{T_w}{T_{t,\infty}}$
y	$\frac{q_w''}{T_{t,\infty}}$

$\frac{\partial m}{\partial y_j}$	$\frac{nx_j - \sum_{j=1}^n x_j}{n \sum_{j=1}^n x_j^2 - (\sum_{j=1}^n x_j)^2}$
$\frac{\partial m}{\partial x_j}$	$\frac{ny_j - \sum_{j=1}^n y_j}{n \sum_{j=1}^n x_j^2 - (\sum_{j=1}^n x_j)^2}$ $- \frac{(n \sum_{j=1}^n x_j y_j - \sum_{j=1}^n x_j \sum_{j=1}^n y_j)(2nx_j - 2 \sum_{j=1}^n x_j)}{[n \sum_{j=1}^n x_j^2 - (\sum_{j=1}^n x_j)^2]^2}$

From the above analysis, the average uncertainty in the endwall heat transfer coefficient was found to be $\pm 9.6\%$ with a confidence interval of 95%. Further insight into Moffat's or Brown's uncertainty methods can be found in the papers cited in the reference section of this Appendix.

References

- [F.1] Moffat, R. J., 1982, "Contributions to the Theory of Single-Sample Uncertainty Analysis," J. Fluids Eng., **104**(2), p. 250.
- [F.2] Brown, K. K., Coleman, H. W., and Steele, W. G., 1998, "A Methodology for Determining Experimental Uncertainties in Regressions," J. Fluids Eng., **120**(3), p. 445.